

**Electronic structure and quantum transport in twisted bilayer graphene with resonant scatterers**Omid Faizy Namarvar <sup>1,2,\*</sup> Ahmed Missaoui <sup>3,4,†</sup> Laurence Magaud,<sup>1,‡</sup>  
Didier Mayou <sup>1,§</sup> and Guy Trambly de Laissardière <sup>4,||</sup><sup>1</sup>*Univ. Grenoble Alpes, CNRS, Institut Néel, 38000 Grenoble France*<sup>2</sup>*XLIM, Univ. Limoges, CNRS UMR 7252, 87000 Limoges, France*<sup>3</sup>*Laboratoire de Spectroscopie Atomique Moléculaire et Applications, Département de Physique, Faculté des Sciences de Tunis, Université Tunis El Manar, Campus Universitaire 1060 Tunis, Tunisia*<sup>4</sup>*CY Cergy Paris Université, CNRS, Laboratoire de Physique Théorique et Modélisation, 95302 Cergy-Pontoise, France*

(Received 5 March 2020; accepted 5 May 2020; published 5 June 2020)

Stacking layered materials revealed to be a very powerful method to tailor their electronic properties. It has indeed been theoretically and experimentally shown that twisted bilayers of graphene (tBLG) with a rotation angle  $\theta$ , forming a Moiré pattern, confine electrons in a tunable way as a function of  $\theta$ . Here, we study electronic structure and transport in tBLG using tight-binding numerical calculations in commensurate twisted bilayer structures and a perturbative continuous theory, which is valid for not-too-small angles ( $\theta > \sim 2^\circ$ ). These two approaches allow us to understand the effect of  $\theta$  on the local density of states, the electron lifetime due to disorder, the DC conductivity, and the conductivity quantum correction due to multiple scattering effects. We distinguish the cases where disorder is equally distributed over two layers or only one layer. When only one layer is disordered, diffusion properties depend strongly on  $\theta$ , thus showing the effect of Moiré electronic localization at intermediate angles  $\theta$ ,  $\sim 2^\circ < \theta < \sim 20^\circ$ .

DOI: [10.1103/PhysRevB.101.245407](https://doi.org/10.1103/PhysRevB.101.245407)**I. INTRODUCTION**

Stacking layered materials is a very powerful method to tailor their electronic properties [1]. The properties not only depend on the choice of materials to be stacked but also on the details of the relative arrangement of the layers. It has thus been theoretically [2–7] and experimentally [8–11] shown that twisted bilayer graphene (tBLG), forming a Moiré pattern, confines conduction electrons in a tunable way as a function of the angle of rotation of one layer with respect to the other. Recently, it has been experimentally proven that this electronic localization by geometry can induce strong electronic correlations [12] and a superconducting state [13] for certain angles called magic angles [6]. Despite numerous studies of the electronic structure of these systems [2–27], the consequences of the electronic localization by a Moiré on electrical transport properties are still poorly known. In particular, the effects of local defects such as adsorbed atoms or adsorbed molecules, which are known to tune strongly electronic properties in graphene-based 2D materials [27–29].

Graphene can be formed in multilayers on SiC [30–38] but also on metal surfaces such as Ni [9] and in exfoliated flakes [8], where hopping terms between successive layers play a crucial role. While on the Si face of SiC, multilayers have an AB Bernal stacking and do not show

graphene properties [30–32,39–43], on the C face, multilayers are twisted multilayers of graphene with various angles of rotation between two successive layers. For large twist angle  $\theta$  between two layers, multilayers show graphenelike properties even when they involve a large number of graphene layers. Indeed, as shown by angle resolved photoemission spectroscopy (ARPES) [35–38], scanning tunneling microscopy (STM) [44], transport [45], and optical transitions [46], their properties are characteristic of a linear graphenelike dispersion. Therefore, in tBLG, interlayer hopping terms do not systematically destroy graphenelike properties but they can lead to the emergence of very peculiar behaviors induced by the Moiré patterns that are accentuated for  $\theta$  smaller than  $\sim 20^\circ$ . Theoretical studies have predicted [2–7,15] the existence of three domains: (1) for large rotation angles ( $\theta > 20^\circ$ ), the layers are decoupled and behave as a collection of isolated graphene layers. (2) For intermediate angles  $\sim 2^\circ < \theta < 20^\circ$ , the dispersion, around Fermi energy  $E_F$ , remains linear but the velocity is renormalized. Consequently, the energies of the two Van Hove singularities (VHSs)  $E_-$  and  $E_+$  are shifted to Dirac energy  $E_D$  when  $\theta$  decreases, as has been shown experimentally [9,10,47,48]. (3) For the lowest  $\theta$ ,  $\theta < \sim 2^\circ$ , almost flat bands appear and result in electronic localization in AA stacking regions: States of similar energies, belonging to the Dirac cones of the two layers, interact strongly. In this regime, the velocity of states at the Dirac point goes to almost zero for specific-angle so-called magic angles [3,6,7]. Recently, the signature of the electron localization in the AA regions at long time evolution has been confirmed numerically for small  $\theta$  [25].

In this paper, we study the consequence of the tunable effective coupling between layers by angle  $\theta$  with interme-

\*omid.faizy@xlim.fr

†ahmed.missaoui@fst.utm.tn

‡laurence.magaud@neel.cnrs.fr

§didier.mayou@neel.cnrs.fr

||guy.trambly@cyu.fr

diate values,  $\sim 2^\circ < \theta < \sim 20^\circ$ , on local density of states (LDOS) and transport properties. We combine tight-binding (TB) numerical calculations for commensurate tBLG and a perturbative continuous theory (see Appendixes) that gives us deeper insights on  $\theta$  effect. Note that our TB calculation includes all matrix element couplings, whereas the continuous theory, like the one previously developed [2,15], neglects the coupling of electrons in different valleys. To analyze transport properties numerically in bulk 2D systems, we consider local defects [49,50], such as adsorbates or vacancies, that are resonant scatterers. Local defects tend to scatter electrons in an isotropic way for each valley and also lead to strong intervalley scattering. The adsorbate is simulated by a simple vacancy in the layer of the  $p_z$  orbital as is usually done [51–53]. Indeed, the covalent bonding between the adsorbate and the carbon atom of graphene to which it is linked eliminates the  $p_z$  orbital from the relevant energy window. We consider here that the up and down spins are degenerate, i.e., we deal with a paramagnetic state. Indeed, the existence and the effect of a magnetic state for various adsorbates or vacancies is still debated [54,55]. In the case of a magnetic state, the up and down spins give two different contributions to the conductivity but the individual contribution of each spin can be analyzed from the results discussed here. We consider the cases (i) where defects are located in the two layers and (ii), where defects are located on one layer (layer 2) only.

In Sec. II, TB LDOS in pristine tBLG and the effect of disorder on total DOS (TDOS) are analyzed with respect to our analytical model for commensurate tBLG. The spatial modulation of the DOS shows an increase of the DOS in the AA region of the Moiré. This is a precursor of the localization in the AA region for very small angles less than  $\sim 2^\circ$  [3,7]. The electrical DC conductivity at high temperature (microscopic conductivity) is studied in Sec. III A, and quantum corrections of conductivity (low-temperature limit) are presented in Sec. III B. The method to compute DC conductivity is given in Appendix A. Numerical results of the paper are analyzed using the analytical continuous model presented in Appendixes B and C. This perturbative theory recovers known results for the velocity renormalization [2,15] but also provides analytical results concerning LDOS and state lifetime versus  $\theta$  values.

The method to build commensurate tBLG is well known and explained in many works. Here we use the same notations as in our previous papers [3,7,16], where each tBLG is built from two indexes  $n$  and  $m$  (Table I). For  $|m - n| = 1$ , the cell of the bilayer contains one Moiré cell, whereas for  $|m - n| > 1$  the cell of the bilayer contains several Moiré cells.

## II. DENSITY OF STATES

### A. Without defect

We first analyze the LDOS in pristine tBLG computed with the TB Hamiltonian detailed in Ref. [7] and the Appendixes. It is now well known theoretically [7,10,15,16] and experimentally [10,48] that the energies  $E_-$  and  $E_+$  of VHSs vary linearly with the angle  $\theta$  for  $\theta > \sim 2^\circ$ . This is clearly seen in the LDOS on the  $p_z$  orbital of an atom located at the center of the AA area of the Moiré (Fig. 1). Since our TB

TABLE I. Studied  $(n, m)$  bilayer structures.  $N$  is the number of atoms,  $\theta$  the rotation angle.

$(n, m)$	$\theta$ [deg.]	$N$
(12,13)	2.656	1876
(10,11)	3.150	1324
(8,9)	3.890	868
(6,7)	5.086	508
(5,6)	6.009	364
(4,5)	7.341	244
(7,9)	8.256	772
(10,13)	8.613	532
(3,4)	9.430	148
(8,11)	10.417	364
(2,3)	13.174	76
(5,9)	18.734	604
(1,3)	32.204	52
(1,4)	38.213	84

Hamiltonian includes coupling beyond the first-neighboring atoms, the electron/hole symmetry is slightly broken and  $E_-$  is not strictly equal to  $-E_+$ .

The LDOS in one layer of the bilayer as a function of position  $\vec{r}$  in the Moiré structure is

$$\rho(E, \vec{r}) = \langle \vec{r} | \delta(E - H) | \vec{r} \rangle. \quad (1)$$

To compare the LDOS in the bilayer with LDOS in the monolayer, we compute the relative variation of the LDOS due to interlayer hopping terms  $\Delta\rho(E, \vec{r})/\rho_m(E)$ , with  $\Delta\rho(E, \vec{r}) = \rho(E, \vec{r}) - \rho_m(E)$ , where  $\rho_m(E)$  is the LDOS in the monolayer that does not depend on the position  $\vec{r}$ .

The LDOS on each carbon atom of Moiré has been calculated using TB, so density map  $\rho(E, \vec{r})$ , where  $\vec{r}$  are the positions of carbon atoms that can be drawn for an energy  $E$ . Figures 2(a.1) and 2(b.1) show relative TB LDOS in (12,13) and (6,7) bilayers at the energy  $E = E_D + 0.05$  eV. The strong increase of LDOS in AA areas with respect to the AB zone are clearly seen. As expected, this difference between LDOS in the AA area and AB area decreases as  $\theta$  increases. Moreover, our numerical TB calculation recovers the difference in the

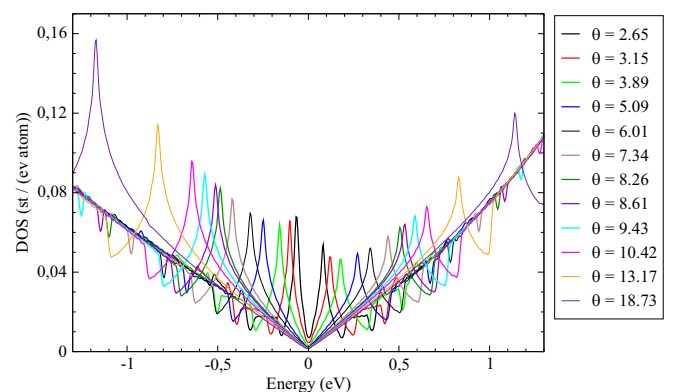


FIG. 1. Local density of states (LDOS) at the center of an AA zone in pristine tBLG listed in Table I for tBLG with different rotation angles  $\theta$  [deg.]. Some LDOS are taken from Ref. [7].  $E_D = 0$ .

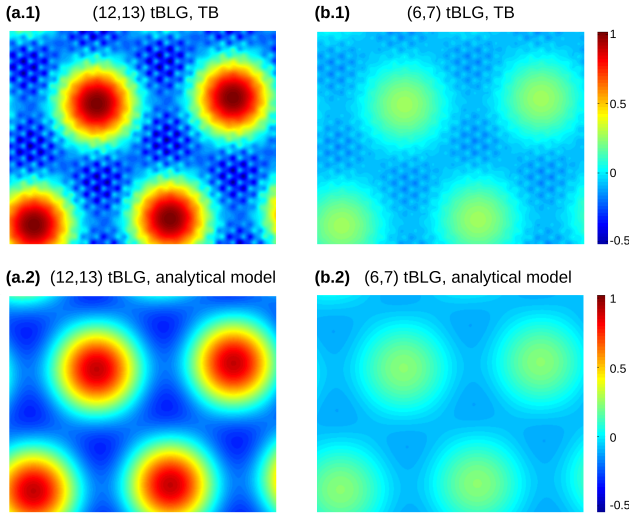


FIG. 2. Relative variation of the LDOS on top layer at energy  $E = E_D + 0.05$  eV, close to the Dirac energy  $E_D$ , in (a) (12,13) tBLG and (b) (6,7) tBLG: (a.1), (b.1) TB results and (a.2), (b.2) analytic results from Eq. (2). To be compared with analytic results, the TB plots are made by a continuous extrapolation of LDOS on atomic orbitals. The same arbitrary units are used for all four LDOS.  $E_D = 0$ .

LDOS of the two inequivalent atoms in the AB area. Indeed, in the AB area, as in AB Bernal stacking, C atoms lying above a C atom of the other layer have a lower LDOS than the LDOS of a C atom not lying above a C atom of the other layer. That leads to a triangular contrast [56] in the density map that has been observed in STM images in AB Bernal bilayers.

According to the perturbative analytical model presented in Appendix C 5, the relative variation of the LDOS is independent of  $E$  for small  $E$  and can be estimated by the simple formula,

$$\frac{\Delta\rho(E, \vec{r})}{\rho_m(E)} \simeq \left(\frac{\theta_1}{\theta}\right)^2 \sum_{j=1}^6 \cos(\vec{G}_j \cdot \vec{r}), \quad (2)$$

where  $\vec{G}_j$  are six equivalent vectors of the reciprocal space of the Moiré lattice. The constant  $\theta_1$  is given by

$$\theta_1 = \frac{\sqrt{2}t}{(\hbar v K_D)}, \quad (3)$$

where  $v$  is the monolayer velocity and  $K_D$  is the modulus of the wave-vector in the Dirac point of graphene. Using the interlayer coupling value  $t \simeq 0.12$  eV (Appendix B 1), one finds that the value of  $\theta_1$  is close to  $\theta_1 \simeq 1^\circ$ . Equation (2) does not depend on the type of atom (A or B) it oscillates with  $\vec{G}_j$  as expected. It is clear the maximum value is obtained for  $\vec{r} = 0$ , which is at the center of the AA area, and relative variation of the LDOS varies as  $\theta^{-2}$ . As shown in Fig. 2, the overall agreement between TB numerical calculation and TB analytical model is very good. We just note a small triangular contrast in the AB zone which is not reproduced by the analytical model (see Appendix Sec. C 5 for a discussion). We observe in particular a reinforcement of the DOS in the AA region and a lowering in the AB regions. This behavior is a precursor of

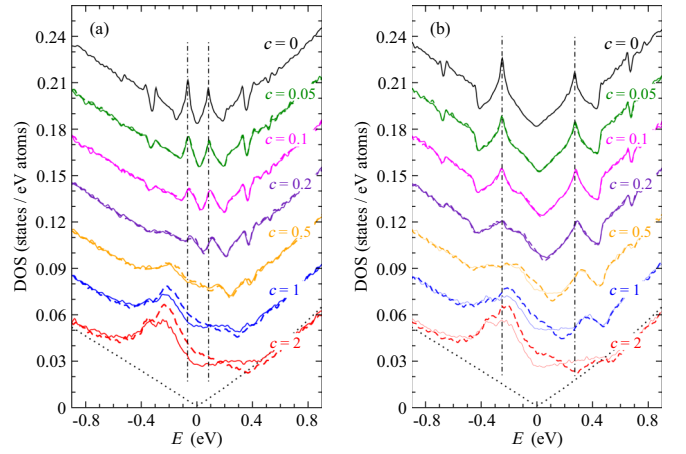


FIG. 3. Total DOS in (a) (12,13) tBLG and (b) (6,7) tBLG, for various concentrations  $c$  (%) of vacancies with respect to the total number of atoms in tBLG. Dashed line: with vacancies in both layers; full line: with vacancies in layer 2. Dotted line is the DOS in pristine monolayer graphene (MLG).  $E_D = 0$ .

the electronic localization in the AA region, which is observed in the very low angle limit  $\theta < \sim 2^\circ$  [3,7,11].

## B. With resonant adsorbates

To study the effect of static defects on the electronic confinement by the Moiré, we include atomic vacancies (vacant atoms) that simulate resonant adsorbates atoms or molecules [52,53,57–62]. For each vacancy concentration  $c$  with respect to the total number of carbon atoms in tBLG, we consider two cases:

- (i) vacancies are randomly distributed in both layers and
- (ii) vacancies are randomly distributed in layer 2 only.

TDOS in (12,13) tBLG and (6,7) tBLG are drawn in Fig. 3 for different concentrations of vacancies in cases (i) and (ii). For small  $c$  values, the VHSs are still clearly seen but they are enlarged by disorder. This shows that static disorder destroys the confinement by Moiré in AA areas. For  $c > \sim 0.5\%$ , peaks of the Van Hove singularities are destroyed by vacancy states. With the TB Hamiltonian including only first-neighbor hopping terms, the vacancy states are midgap states at Dirac energy [57,58]. But, as in monolayer graphene [60] and Bernal bilayer graphene [53], taking into account the TB hoppings beyond first neighbor enlarges the midgap states and shifts it to negative energies, typically around  $-0.2$  eV. As shown in Fig. 4, when vacancies are located in layer 2 only [case (ii)], the vacancy states only appear on LDOS  $p_z$  orbitals of layer 2. Note that average DOS in layer 1 is slightly modified by the vacancies located in layer 2 (Fig. 4). This effect seems similar to modification due to nonresonant scatterers [52]. Figures 3 and 4 show that, as far as the DOS is concerned and for rather large concentrations of vacancies ( $c > 0.5\%$ ), the rotated angle  $\theta$  does not change the effect of vacancies. As we will see in the next section, the effect of  $\theta$  is more pronounced on wave-packet quantum diffusion and thus on transport properties.

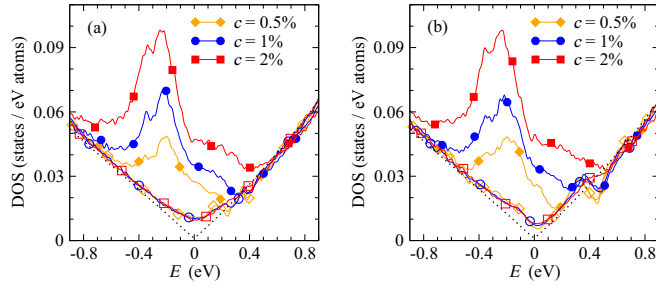


FIG. 4. Average LDOS in each layer: (a) (12,13) tBLG and (b) (6,7) tBLG, for various concentrations  $c$  (%) of vacancies in layer 2. Empty symbol: average LDOS in layer 1; full symbol: average LDOS in layer 2. Dotted line is the DOS in pristine monolayer graphene (MLG).  $c$  is the concentration of vacancies with respect to the total number of atoms in tBLG.  $E_D = 0$ .

### III. QUANTUM TRANSPORT

Within the Kubo-Greenwood formalism, we compute the conductivity  $\sigma(E_F)$  versus the Fermi energy  $E_F$  using the real-space method developed by Mayou, Khanna, Roche, and Triozon [63–67] in the framework of the relaxation time approximation (RTA) to account [52] effects of inelastic scatterers due to electron-phonon interactions (see Appendix A). Elastic-scattering events due to local defects (vacant atoms) are included in the Hamiltonian itself in a large unit cell containing more than  $10^7$  atoms with boundary periodic conditions.

#### A. High-temperature conductivity

We first consider the high-temperature case (or room-temperature case) where the inelastic-scattering time  $\tau_i$  is close to the elastic-scattering time  $\tau_e$  due to static defects. In that case, the DC conductivity is called *microscopic conductivity*,  $\sigma_M$ , because it takes into account quantum interference effects occurring during time less or equal to  $\tau_e \simeq \tau_i$ .  $\sigma_M$  is close to semiclassical conductivity that does not take into account the quantum corrections due to multiple scattering effects. Typically, this quantity represents a room-temperature conductivity when multiple scattering effects are destroyed by dephasing due to the electron-phonon interactions. In Fig. 5,  $\sigma_M(E)$  is shown for three tBLG (12,13), (6,7), and (3,4), with rotated angle  $\theta$  equal to  $2.656^\circ$ ,  $5.086^\circ$ , and  $9.430^\circ$ , respectively, and in Fig. 6,  $\sigma_M(\theta^2)$  is shown for different energy values close to the Dirac energy  $E_D$ .

For vacancy distribution (i), i.e., vacancies randomly distributed in two layers,  $\sigma_M(E)$  is almost independent of  $\theta$  value. When vacancy concentration  $c$  is large (Fig. 6,  $c = 1\%$  and  $2\%$ ) behavior is similar to that of MLG and  $\sigma_M \simeq 2\sigma_{M,MLG}$ , where  $\sigma_{M,MLG}$  is the conductivity for MLG [52],  $\sigma_{M,MLG} \simeq 0.6 G_0$ , with  $G_0 = 2e^2/h$ .  $\sigma_{M,MLG}$  reaches the well-known universal minimum of the so-called conductivity “plateau”—independent of defect concentration—at energies around  $E_D$  [51]. For smaller concentrations (Fig. 6,  $c = 0.5\%$ ),  $\sigma_M$  increases when the concentration  $c$  increases. These two regimes are similar to the one found in AB Bernal bilayer graphene [53]. Roughly speaking, for large  $c$  values, the elastic mean-free path  $L_e$  in MLG (see Fig. 4(a) in

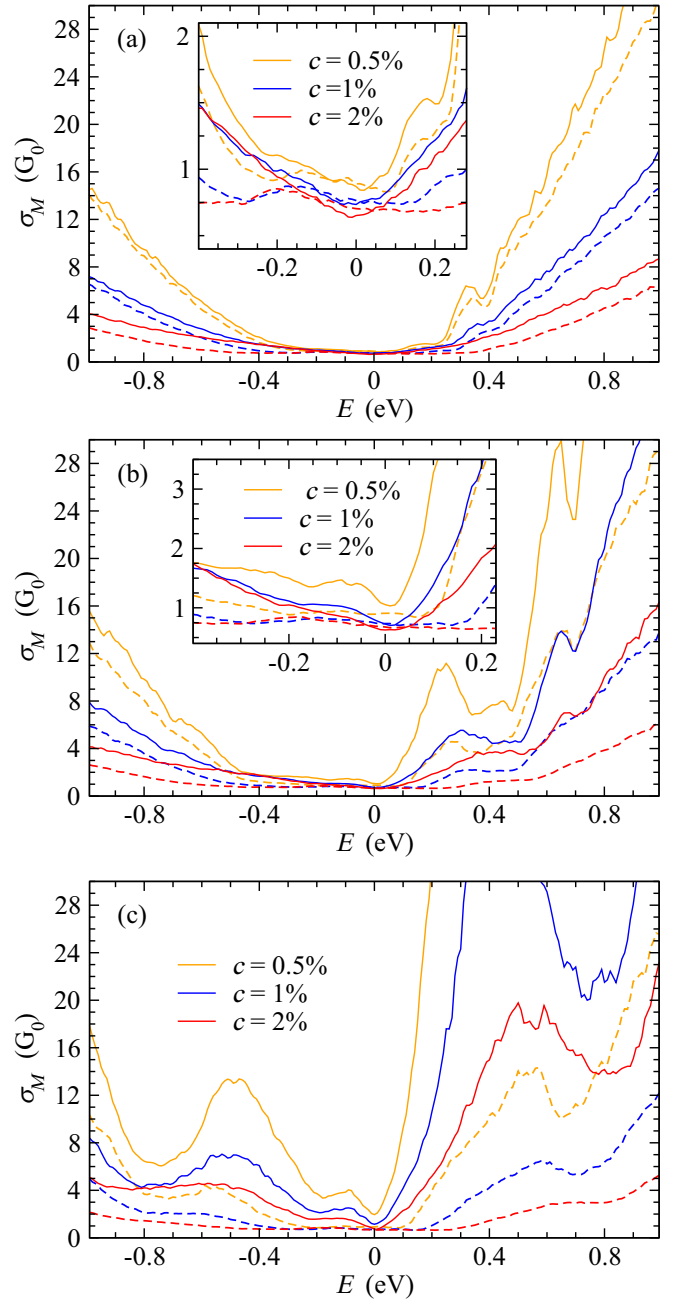


FIG. 5. Microscopic conductivity  $\sigma_M$  in (a) (12,13) tBLG, (b) (6,7) tBLG, (c) (3,4) tBLG, for the two cases: (Full line) with vacancies in layer 2 and (dashed line) with vacancies in both layers.  $c$  is the concentration of vacancies with respect to the total number of atom in tBLG. Inserts:  $\sigma_M$  around the Dirac energy  $E_D = 0$ .

Ref. [53]) is smaller than the average traveling distance [53]  $l_1$  in a layer between two interlayer hoppings of the charge carriers, and thus carriers behaves as in MLG. Whereas, for small  $c$  values,  $L_e > l_1$  and thus interlayer hopping are involved in the diffusive regime and BLG conductivity properties are different than MLG ones.

For vacancy distribution (ii), i.e., vacancies randomly distributed in layer 2, and a large rotated angle [Fig. 5(c)], conductivity is larger than in case (i). Indeed, for large  $\theta$ , typically  $\theta > 10^\circ$ , eigenstates are located mainly in one layer

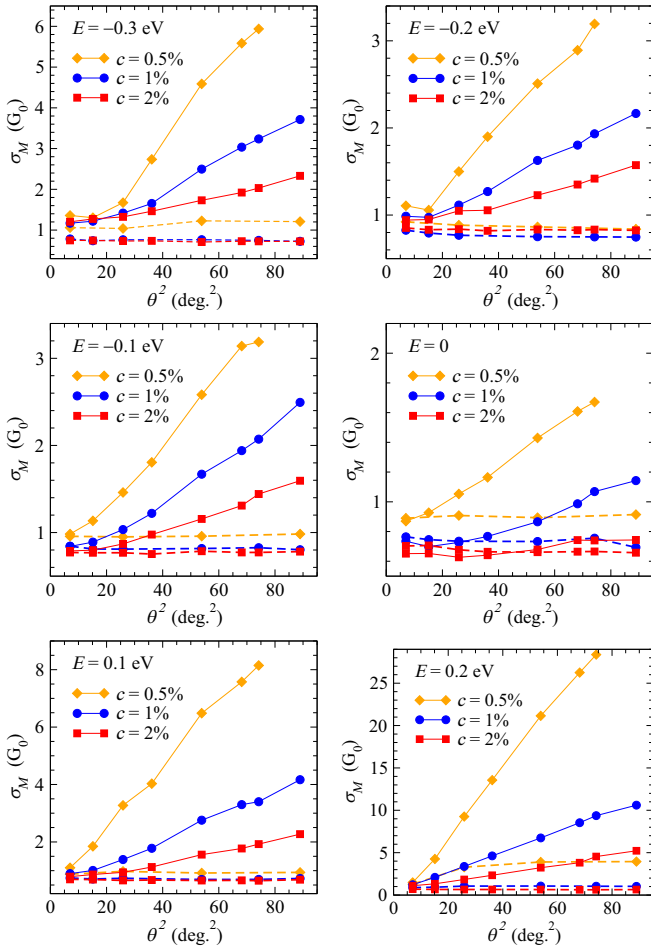


FIG. 6. Microscopic conductivity  $\sigma_M$  in tBLG versus rotated angle  $\theta^2$  for energy values  $E$ . Full line: with vacancies in layer 2; dashed line: with vacancies in both layers.  $c$  is the concentration of vacancies with respect to the total number of atoms in tBLG.  $E_D = 0$ .

(decoupled layers) [3,16] and thus conductivity of the bilayer is the sum of the conductivity of two almost independent layers,

$$\sigma_M \simeq \sigma_{M,1} + \sigma_{M,2}, \quad (4)$$

corresponding to conductivity of layers 1 and 2, respectively. The conductivity of a layer with defects is close to MLG conductivity  $\sigma_{M,2} \simeq \sigma_{M,MLG}$  and the conductivity of a layer without defects  $\sigma_{M,1}$  is affected by the presence of defects in layer 2. With increasing  $\theta$ , the eigenstates are more and more located on one layer, thus layers are more and more decoupled, and the  $\sigma_{M,1}$  increases as layer 1 becomes more and more like a pristine MLG. Consequently, the conductivity of the tBLG increases when  $\theta$  increases. In these cases, numerical results (Fig. 6) show that  $\sigma_M$  increases as  $\theta^2$ .

For small angles [Figs. 5(a) and 6], eigenstates are located almost equally on both layers for all energies around Dirac energy [16]; therefore, they are affected in a similar way by the two kinds of vacancies distributions (i) and (ii). Conductivity is thus very similar in the two cases.

The analytical model presented in Appendix C 4 allows us to understand why  $\sigma_M$  increases as  $\theta^2$  when defects are located

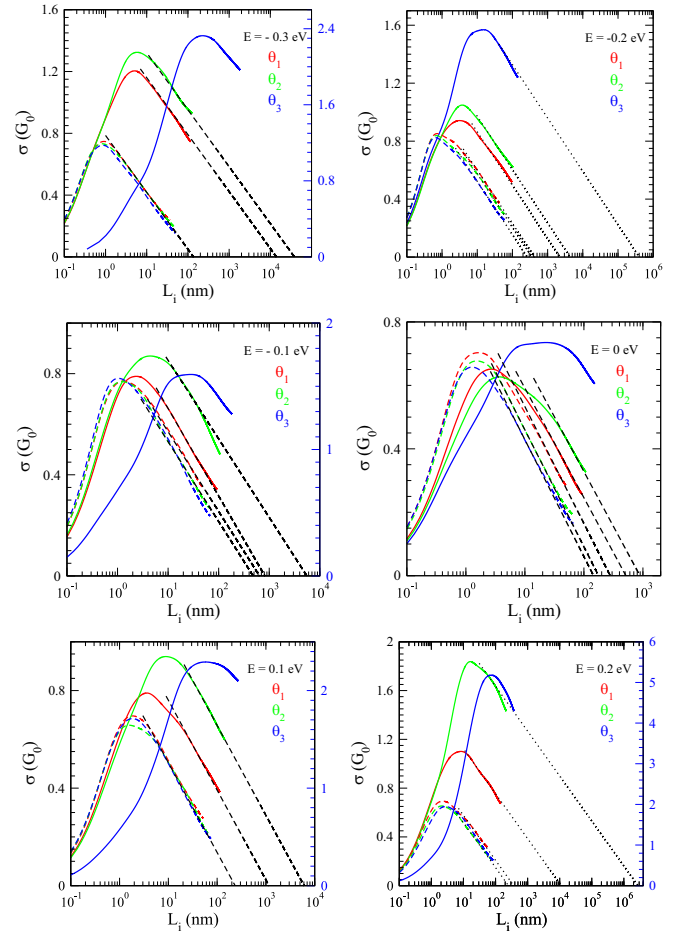


FIG. 7. Conductivity in bilayer versus inelastic scattering  $L_i$ , at the energies  $E$ , for concentration  $c = 2\%$  of vacancies with respect to the total number of atoms in bilayer: ( $\theta_1 = 2.656^\circ$ ) (12,13) tBLG, ( $\theta_2 = 5.086^\circ$ ) (6,7) tBLG, ( $\theta_3 = 9.430^\circ$ ) (3,4) tBLG. Line: with vacancies in layer 2; dashed line: with vacancies in both layers. For (3,4) tBLG ( $\theta_3 = 9.430^\circ$ ), the localization regime appears at very large times for which very time-consuming calculations are necessary; that is why this regime is only roughly estimated by extrapolation.

only in layer 2 [case (ii)]. From Einstein conductivity formula, conductivity in layer  $p$ ,  $p = 1, 2$ , is

$$\sigma_{M,p}(E) = e^2 \rho_p(E) v^2 \tau_p, \quad (5)$$

where  $\rho_p$  and  $\tau_p$  are the average DOS in layer  $p$  and the average elastic-scattering time in layer  $p$ , respectively. For energy values in the plateau of conductivity around  $E_D$ , layer 2—with defects—has a conductivity close to the universal minimum of MLG [52],  $\sigma_{M,2}(E) \simeq \sigma_{M,MLG}$ , thus, from Eqs. (4) and (5), the conductivity in the bilayer is

$$\sigma_M(E) \simeq \sigma_{M,MLG} \left( 1 + \frac{\rho_1(E) \tau_1}{\rho_2(E) \tau_2} \right), \quad (6)$$

where the ratio between scattering times can be estimated from the formula Eq. (C18) obtained in the Appendixes. Thus,

$$\sigma_M(E) \simeq \sigma_{M,MLG} \left( 1 + \frac{\rho_1(E) \theta^2}{\rho_2(E) \theta_0^2} \right), \quad (7)$$

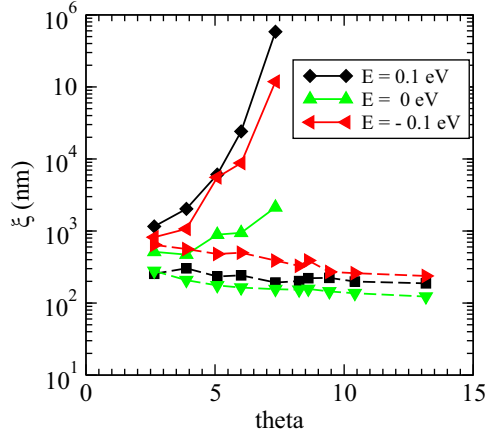


FIG. 8. Localization length versus angle  $\theta$ , at the energies  $E$ , for concentration  $c = 2\%$  of vacancies with respect to the total number of atoms in the bilayer. Line: with vacancies in layer 2; dashed line: with vacancies in both layers.

with  $\theta_0$  related to  $\theta_1$  [Appendix Eq. (C2)],

$$\theta_0 = \sqrt{3}\theta_1, \quad (8)$$

i.e.,  $\theta_0 \simeq 2^\circ$  (Appendix C3). Since  $\rho_1(E)$  and  $\rho_2(E)$  are different (Fig. 4) and depend on the energy values and the defect concentration  $c$ , the slope of  $\sigma_M$  versus  $\theta^2$  also depends on  $E$  and  $c$  (Fig. 6).

### B. Low-temperature conductivity

In the low-temperature limit, inelastic-scattering time  $\tau_i$  is larger than elastic-scattering time  $\tau_e$ , and multiple scattering effects may reduce the conductivity with respect to microscopic conductivity  $\sigma_m$ . The average inelastic length  $L_i$  thus satisfies  $L_i \gg L_e$  and  $L_i \gg l_1$ .  $\tau_i$  and  $L_i$  increase when temperature decreases. To evaluate this effect, we compute [52,53] the conductivity  $\sigma$  versus  $L_i$  at every energy  $E$  (Fig. 7) for the two vacancy distribution cases: (i) in two layers and (ii) in layer 2. As expected in disordered 2D systems [68], for large  $L_i$ ,  $\sigma(L_i)$  follows a linear variation with the logarithm of  $L_i$ , like in the case of monolayer graphene [52,69] and Bernal bilayer graphene [53]

$$\sigma(E, L_i) = \sigma_0 - \alpha G_0 \ln(L_i), \quad (9)$$

where  $\sigma_0$  is a constant depending on  $\sigma_M$  and  $L_e$ , and slope  $\alpha$  is almost independent on energy  $E$ , the defect concentration, and the repartition of the defects (in one layer or in both layers). From numerical results, one obtains  $\alpha \simeq 0.32$  which is close to the monolayer value [52] and Bernal bilayer value [53].

Localization length  $\xi$  can be estimated from the equation  $\sigma(L_i = \xi) = 0$  and the linear extrapolation of  $\sigma$  versus  $\log L_i$  at large  $L_i$  (see dashed lines Fig. 7).  $\xi$  versus  $\theta$  for various energies in the plateau of conductivity are shown in Fig. 8. As  $\sigma_M$ ,  $\xi$  is almost independent of  $\theta$  when defects are located in both layers, but  $\xi$  increases strongly when defects are located in one layer only.

## IV. CONCLUSION

We have presented a numerical study of the LDOS and the conductivity in pristine and covalently functionalized tBLGs, with an angle of rotation  $\theta > 2^\circ$ . Those results are understood using a perturbative analytical model described in the Appendixes. The atomic structure in Moiré induces a strong modulation in the LDOS between AA stacking areas and AB stacking areas, which varies as  $\theta^{-2}$ , following a simple analytic expression. We show that disorder breaks the interlayer effective coupling due to the Moiré pattern. Therefore, when defects are randomly distributed in both layers, the conductivity  $\sigma_M$  is almost independent of  $\theta$ , whereas  $\sigma_M \sim \theta^2$  when defects are randomly distributed in one layer only. Such a nonsymmetric distribution of defects may often occur in experimental situations because of the effects of substrate, adatoms, or admolecules. Finally, the quantum correction to the conductivity is computed and localization length is calculated versus  $\theta$ .

## ACKNOWLEDGMENTS

The authors wish to thank C. Berger, W. A. de Heer, P. Mallet, J.-Y. Veullen, T. Le Quang, V. Renard, and C. Chapelier for fruitful discussions. TB calculations were performed at the Centre de Calculs (CDC), Université de Cergy-Pontoise. We thank Y. Costes and Baptiste Mary, CDC, for computing assistance. DFT calculations were performed using HPC resources from GENCI-IDRIS (Grants No. A0060910784 and No. A0060907655). This work was supported by ANR (FR), J2D (ANR-15-CE24-0017), and the Paris//Seine excellence initiative (Grant No. 2019-055-C01-A0).

## APPENDIX A: KUBO-GREENWOOD CONDUCTIVITY

In the Kubo-Greenwood approach for transport properties, the quantum diffusion  $D$  is computed by using the polynomial expansion of the average square spreading,  $\Delta X^2$ , for charge carriers. This method, developed by Mayou, Khanna, Roche and Triozon [63–67], allows for very efficient numerical calculations by recursion in real space that takes into account all quantum effects. Static defects are included directly in the structural modelization of the system and they are randomly distributed on a supercell containing up to  $10^7$  carbon atoms. Inelastic scattering is computed [52] within the RTA, including an inelastic-scattering time  $\tau_i$  beyond which the propagation becomes diffusive due to the destruction of coherence by inelastic processes. One finally gets the Einstein conductivity formula [52],

$$\sigma(E_F, \tau_i) = e^2 \rho(E_F) D(E_F, \tau_i), \quad (A1)$$

where  $E_F$  is the Fermi level,  $D(E, \tau_i)$  is the diffusivity (diffusion coefficient at energy  $E$  and inelastic scattering time  $\tau_i$ ),

$$D(E, \tau_i) = \frac{L_i^2(E, \tau_i)}{2\tau_i}, \quad (A2)$$

$\rho(E)$  is the DOS and  $L_i(E, \tau_i)$  is the inelastic mean-free path.  $L_i(E, \tau_i)$  is the typical distance of propagation during the time

interval  $\tau_i$  for electrons at energy  $E$ :

$$L_i^2(E, \tau_i) = \frac{1}{\tau_i} \int_0^\infty \Delta X^2(E, t) e^{-t/\tau_i} dt. \quad (\text{A3})$$

Without static defects (static disorder), the  $L_i$  and  $D$  goes to infinity when  $\tau_i$  diverges. With statics defects, at every energy  $E$ ,  $\sigma(\tau_i)$  reaches a maximum value,

$$\sigma_M(E_F, \tau_i) = e^2 n(E_F) \text{Max}_{\tau_i} \{D(E_F, \tau_i)\}, \quad (\text{A4})$$

called *microscopic conductivity*.  $\sigma_M$  corresponds to the usual semiclassical approximation (semiclassical conductivity). This conductivity is typically the conductivity at room temperature, when inelastic-scattering time  $\tau_i$  (inelastic mean-free path  $L_i$ ) is close to elastic-scattering time  $\tau_e$  (elastic mean-free path  $L_e$ ),  $\tau_e(E) = L_e(E)/v(E)$  and  $L_e(E) = D_M(E)/2v(E)$ , where  $D_M(E)$  is the maximum value of  $D(\tau_i)$  at energy  $E$  and  $v(E)$  the velocity at very small times [slope of  $\Delta X(t)$ ].

For larger  $\tau_i$  and  $L_i$ ,  $\tau_e \ll \tau_i$  and  $L_e \ll L_i$ , quantum interferences may result in a diffusive state,  $D(\tau_i) \simeq D_M$ , or a subdiffusive state where  $D$  decreases when  $\tau_i$  and  $L_i$  increase. For very large  $L_i$ ,  $L_i$  close to localization length  $\xi$ , the conductivity goes to zero.

## APPENDIX B: TIGHT-BINDING MODEL

### 1. Real-space couplings

In the TB scheme, only  $p_z$  orbitals are taken into account since we are interested in electronic states close to the Fermi level. The TB model used in this paper is the same as in our previous work on twisted bilayer graphene [3,7,16] and AB Bernal bilayer graphene [53,62]. The Hamiltonian has the form

$$H = \sum_i \epsilon_i |i\rangle \langle i| + \sum_{(i,j)} t_{ij} |i\rangle \langle j|, \quad (\text{B1})$$

where  $i$  is the  $p_z$  orbital located at  $\vec{r}_i$  with an on-site energy  $\epsilon_i$ , and the sum runs over all neighboring  $i, j$  sites.  $t_{ij}$  is the hopping element matrix between site  $i$  and site  $j$ , computed from the usual Slater-Koster parameters as given in Ref. [7]. Since the layers are rotated, interlayer neighbors are not on top of each other (as is the case for the Bernal AB stacking). Therefore, the interlayer hopping terms are then not restricted to  $pp\sigma$  terms but  $pp\pi$  terms also have to be introduced [3,7]. Moreover, hopping terms are not restricted to first-neighboring orbitals and they decrease exponentially with the interatomic distance. A cutoff distance  $r_c$  is introduced which must be large enough so the results do not depend on it. We have checked that  $r_c = 0.6$  nm is enough. For small  $r_c$  values, a small gap may appear at the Dirac energy as shown in Fig. 9. Several studies [70–73] have shown that this small gap comes from nonzero matrix element coupling electron states in equivalent Dirac cones for some superstructures with a small number of atoms in the cell of tBLG.

The matrix element of the interlayer Hamiltonian  $H_c$  between one orbital at  $\vec{r}$  in layer 1 and one orbital at  $\vec{r}'$  in layer 2 is given by

$$\langle \vec{r}' | H_c | \vec{r} \rangle = H_c(|\vec{r} - \vec{r}'|). \quad (\text{B2})$$

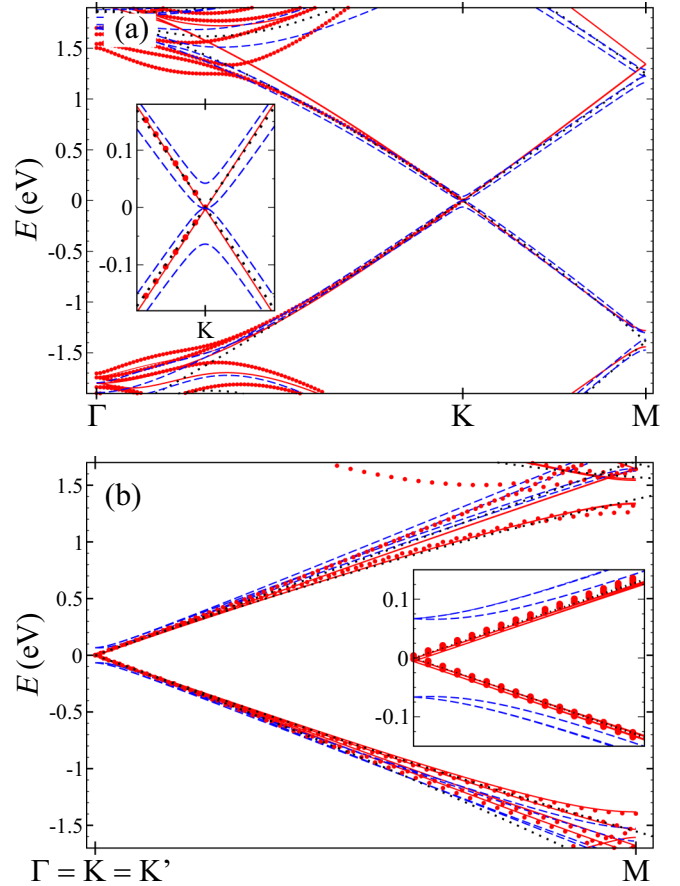


FIG. 9. Band dispersion  $E(\vec{k})$ . Red points: DFT calculation using VASP code (for details on the calculation, see Ref. [7]); red lines: TB calculation, for (a) (1,3) tBLG ( $\theta = 32.20^\circ$ ), (b) (1,4) tBLG ( $\theta = 38.21^\circ$ ), calculated with a large interlayer cutoff distance  $r_c = 0.60$  nm, whereas blue dashed line shows TB bands with a too-small  $r_c$ ,  $r_c = 0.34$  nm. In the latter case, a nonphysical gap appears at energy  $E_D = 0$ . Dotted black line is for MLG. Insert: Zoom of the bands around the K point.  $E_D = 0$ .

Note that  $H_c(\vec{r} - \vec{r}')$  is real and depends only on the modulus  $|\vec{r} - \vec{r}'|$ .  $H_c(|\vec{r}|)$  is maximum at zero distance, i.e., when the two orbitals are aligned perpendicularly to the two layers. The hopping integral between the two orbitals decreases when their distance increases. The Fourier transform, which will be essential in the following, is also real and depends only on the modulus of the wave vector. From the Fourier transformation, we write

$$H_c(\vec{r}) = \int \tilde{H}_c(\vec{k}) e^{i\vec{k}\cdot\vec{r}} d^2\vec{k} \quad (\text{B3})$$

and

$$\tilde{H}_c(\vec{k}) = \frac{1}{(2\pi)^2} \int H_c(\vec{r}) e^{-i\vec{k}\cdot\vec{r}} d^2\vec{r}. \quad (\text{B4})$$

Here too the coupling  $\tilde{H}_c(\vec{k})$  decreases when  $|\vec{k}|$  increases. We shall see below that the largest value of  $\tilde{H}_c(\vec{k})$  is for  $|\vec{k}|$  close to the modulus of a Dirac point which is represented by  $K_D$  in Fig. 10.

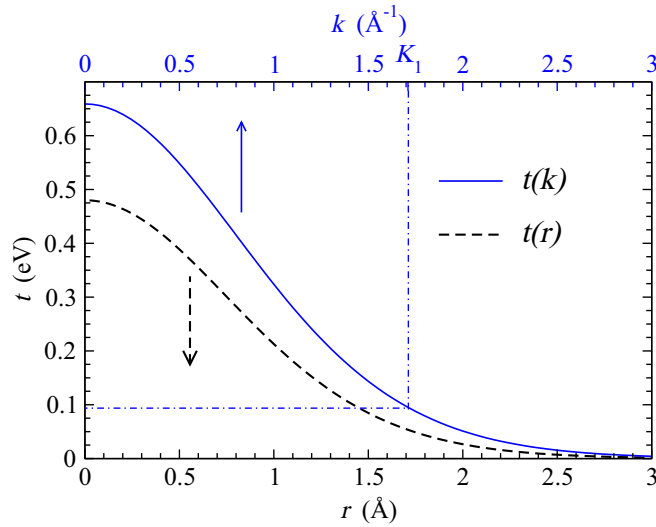


FIG. 10. Modulus of the interlayer coupling  $t$  versus inlayer distance  $r$  and modulus  $k$  of the wave vector, calculated from the tight-binding model described in Ref. [7].

## 2. Interlayer coupling between Bloch states

We want to compute the coupling between two Bloch states of layer 1 and layer 2. Each graphene layer is a honeycomb lattice with two atoms, A and B, in its unit cell. Let us consider normalized Bloch states made of atomic  $p_z$  orbitals A or B in layer  $\alpha$ ,  $\alpha = 1$  or 2,

$$|A\vec{k}\rangle_\alpha = \frac{1}{\sqrt{N}} \sum_{\vec{R}} e^{i\vec{k}\cdot\vec{R}_A} |A\vec{R}\rangle_\alpha, \quad (\text{B5})$$

$$|B\vec{k}\rangle_\alpha = \frac{1}{\sqrt{N}} \sum_{\vec{R}} e^{i\vec{k}\cdot\vec{R}_B} |B\vec{R}\rangle_\alpha, \quad (\text{B6})$$

where  $N$  is the number of unit cells of the crystal and the summation is performed on all cells of crystal ( $\vec{R}$ ). In the following, A or B are indicated by  $\varepsilon$  according to the following convention:

$$\varepsilon = \begin{cases} \text{A} & \text{for A atom} \\ \text{B} & \text{for B atom,} \end{cases} \quad (\text{B7})$$

$$\alpha = \begin{cases} 1 & \text{lower layer} \\ 2 & \text{upper layer.} \end{cases} \quad (\text{B8})$$

The positions of the atoms in layer 1 are

$$\begin{cases} \vec{r}_{\varepsilon\vec{R}} = \vec{R} & \text{if } \varepsilon = \text{A} \\ \vec{r}_{\varepsilon\vec{R}} = \vec{R} + \vec{u} & \text{if } \varepsilon = \text{B} \end{cases} \quad (\text{B9})$$

and, in layer 2,

$$\begin{cases} \vec{r}'_{\varepsilon'\vec{R}'} = \vec{R}' & \text{if } \varepsilon' = \text{A} \\ \vec{r}'_{\varepsilon'\vec{R}'} = \vec{R}' + \vec{u}' & \text{if } \varepsilon' = \text{B,} \end{cases} \quad (\text{B10})$$

where  $\vec{u}$  and  $\vec{u}'$  are vectors connecting the two atoms in the unit cells, i.e., A and B atoms in layer 1 and A' and B' atoms in layer 2, respectively. Writing

$$H_c |\varepsilon\vec{k}\rangle_2 = \sum_i t(\varepsilon_i\vec{k}_i, \varepsilon\vec{k}) |\varepsilon_i\vec{k}_i\rangle_1, \quad (\text{B11})$$

where  $t(\varepsilon_i\vec{k}_i, \varepsilon\vec{k}) \equiv t_i$  is the transfer matrix element, we find a selection rule such that

$$\vec{k} + \vec{K}_r = \vec{k}' + \vec{K}'_r, \quad (\text{B12})$$

where  $\vec{K}_r$  and  $\vec{K}'_r$  are vectors of reciprocal lattices. This means that interlayer coupling Hamiltonian  $H_c$  couples the upper state  $|\varepsilon\vec{k}\rangle_2$  to lower state  $|\varepsilon\vec{k}\rangle_1$  only if the selection rule Eq. (B12) is obeyed.

Finally, for  $\vec{k}_i = \vec{k} + \vec{K}_r = \vec{k}' \pmod{\vec{K}'_r}$ , we derive a formula for the coupling matrix; after some calculations [74], we switch to the following expression of the Hamiltonian:

$$t_i(\vec{k} + \vec{K}_r) = \frac{4\pi^2}{S} \tilde{H}_c(\vec{k} + \vec{K}_r) e^{i(\vec{k} + \vec{K}_r) \cdot (\varepsilon'\vec{u}' - \varepsilon\vec{u} + \vec{\Delta})}. \quad (\text{B13})$$

$S$  is the area of the unit cell,  $\vec{\Delta}$  is the translation between the two layers. However, this translation of the two layers just translates the overall Moiré pattern and can be set to zero without loss of generality.

By symmetry of hopping term between two orbitals, coupling depends only on the modulus of  $\vec{k} + \vec{K}_r$ , i.e.,  $\tilde{H}_c(\vec{k} + \vec{K}_r) \simeq \tilde{H}_c(|\vec{K}_D + \vec{K}_r|)$ , in the vicinity of the Dirac point. The modulus of  $t_i$  is represented in Fig. 10. One sees that the largest value of  $|t_i|$  is one that corresponds to the smallest possible value of  $|\vec{k} + \vec{K}_r|$ . By careful examination, it can be shown that for electronic states close to the Dirac point, this minimum corresponds to the modulus of the wave vector in the Dirac point ( $K_D = \|\vec{K}_D\| \simeq 17.2 \text{ nm}^{-1}$ ). From Fig. 10, it is easy to deduce numerically the interlayer hopping term close to Dirac is around  $t_1 \simeq 0.12 \text{ eV}$ . All the other contributions are much smaller and will be neglected here.

Selecting only this contribution means that  $\vec{K}_r$  is such that  $\vec{k} + \vec{K}_r$  belongs to one of three equivalent valleys. Therefore, a set of two Bloch states with a given wave vector [Eqs. (B5) and (B6)] in one layer will be coupled to three sets of two Bloch states in other layers corresponding to three different wave vectors. This strongly simplifies the structure of the Hamiltonian and the analytical calculations presented here.

In the following, we shall count the vectors  $\vec{k}$  and  $\vec{k}'$  from their respective Dirac points  $\vec{K}_{D1}$  and  $\vec{K}'_{D1}$ .  $\vec{K}_{D1}$  is obtained from  $\vec{K}_D$  by a rotation of an angle  $\theta$  around the vector  $\vec{\zeta}$  which is perpendicular to layers 1 and 2. Therefore, one has

$$\vec{k} = \delta\vec{k} + \vec{K}_{D1}, \quad (\text{B14})$$

$$\vec{k}' = \delta\vec{k}' + \vec{K}'_{D1}. \quad (\text{B15})$$

Finally, one gets for the selection rule

$$\delta\vec{k}' \simeq \delta\vec{k} - \theta\vec{\zeta} \times \vec{K}_{Di}, \quad (\text{B16})$$

where the index  $i$  takes the values  $i = 1, 2, 3$ .  $\vec{K}_{Di}$  and  $\vec{K}'_{Di}$  are the three equivalent Dirac points in layers 1 and 2.  $\vec{K}'_{Di}$  is obtained from  $\vec{K}_{Di}$  by a rotation of an angle  $\theta$  around the vector  $\vec{\zeta}$ .

## APPENDIX C: EFFECT OF INTERLAYER COUPLING

We consider layer 1 coupled to layer 2, which is rotated by an angle  $\theta$  with respect to layer 1. If one considers the time evolution within layer 1 or, more generally, the restriction of

the total Green's function to layer 1, the coupling to layer 2 amounts to the addition of an effective Hamiltonian or self-energy. From this effective Hamiltonian, we shall get the velocity renormalization, the electron lifetime in layer 1 due to disorder in layer 2, and the modulation of the DOS close the charge neutrality point. The theory which is developed here is perturbative and assumes that the rotation angle  $\theta$  is not too small. In particular, we emphasize that the perturbation theory is valid for

$$z, t, \Delta \ll \hbar v K_D \theta, \quad (\text{C1})$$

where  $v$  is the monolayer velocity and  $K_D = \|\vec{K}_D\|$ ,  $z$  is the energy of calculation,  $t$  is the interlayer coupling ( $t \simeq t_1 \simeq 0.12$  eV, Appendix B 1) and  $\Delta$  is a possible difference in on-site energy between the two layers. The condition on  $t$  implies that  $\theta > \theta_1$ , where

$$\theta_1 = \frac{\sqrt{2}t}{(\hbar v K_D)}. \quad (\text{C2})$$

The value of  $\theta_1$  is close to  $\theta_1 \simeq 1^\circ$ . The condition on  $z$  implies that the current energy at which the quantities are calculated is smaller than the typical energy of the VHSs, which depends linearly on  $\theta$ . The difference in energy  $\Delta$  of the two layers must also be smaller than the energy of the VHS. Note that the VHSs have been clearly observed with STM experiments on twisted graphene bilayer [10].

### 1. Effective one-plan Hamiltonian

We consider first a Bloch state in layer 1 with wave vector  $\delta\vec{k}_0$ . It can be coupled to a Bloch state  $\delta\vec{k}'$  in layer 2, then propagates freely in layer 2, and is scattered again to a Bloch state in layer 1 with a wave vector  $\delta\vec{k}_f$ . Applying the selection rule Eq. (B16) to each interlayer hopping term, we find that  $\delta\vec{k}_f$  and  $\delta\vec{k}_0$  are related by

$$\delta\vec{k}_f \simeq \delta\vec{k}_0 - \theta \vec{\zeta} \times (\vec{K}_{Di} - \vec{K}_{Dj}). \quad (\text{C3})$$

Therefore, the coupling between layers 1 and 2 induces an effective coupling between Bloch states of layer 1 with the selection rule Eq. (C3). Note that the indices  $i$  and  $j$  take the values 1, 2, 3.

When  $i = j$ , a Bloch state with  $\delta\vec{k}_0$  is coupled only to the Bloch states with the same wave-vector  $\delta\vec{k}_f = \delta\vec{k}_0$ . This process gives a self-energy which renormalizes the energy of the state of the single layer 1 (see below).

When  $i$  and  $j$  are different, then  $\delta\vec{k}_f$  and  $\delta\vec{k}_0$  are different:

$$\delta\vec{k}_f \simeq \delta\vec{k}_0 + \vec{G}_k. \quad (\text{C4})$$

$\vec{G}_k = \theta \vec{\zeta} \times (\vec{K}_{Di} - \vec{K}_{Dj})$  is a reciprocal lattice vector of the Moiré lattice, where  $\vec{K}_{Di} - \vec{K}_{Dj}$  is a reciprocal lattice vector of graphene. These vectors take six possible values, named  $\vec{G}_k$  in the main text, that are vectors of the reciprocal lattice of the Moiré pattern. As we show below, this coupling between Bloch states of different wave vectors will create eigenstates with mixing of different oscillating components which leads to oscillations in the DOS with wave-vector components  $\vec{G}_k$  (see below). We note also that the coupling introduces only small spatial frequencies and in particular it does not connect states of the two nonequivalent Dirac cones.

### 2. Self-energy

We are interested in the self-energy of coupling of states in layer 1 due to the coupling with states of layer 2. Indeed, the real part of self-energy  $\Re\sigma(z)$  is associated to the modification of the dispersion relation and will allow us to discuss velocity renormalization. The imaginary part of self-energy is associated to the electron lifetime. It will allow us to discuss the lifetime of the electron in one layer when there is disorder in another layer.

Using matrix notations defined in Appendix B, we have

$$\tilde{\Sigma}_1(z) = \sum_{\vec{K}_r} T_+(\vec{K}_r) \mathcal{G}_2(\vec{K}_D + \vec{K}_r) T_-(\vec{K}_r), \quad (\text{C5})$$

where  $\vec{K}_r$  is the vector of reciprocal lattice which has three values that connect one Dirac point to itself or to the two other equivalent Dirac points.  $T$  describes the coupling between two layers and the Green's operator at wave vector  $\theta \vec{\zeta} \times \vec{K}_{d\mu}$  is

$$\mathcal{G}_2(z, \theta \vec{\zeta} \times \vec{K}_{d\mu}) = \frac{1}{z - H_-(\theta \vec{\zeta} \times \vec{K}_{d\mu})}, \quad (\text{C6})$$

where  $\vec{K}_{d\mu}$  counts the three equivalent Dirac points. And for the Hamiltonian [74],

$$H_2(\theta \vec{\zeta} \times \vec{K}_{d\mu}) = \begin{pmatrix} \Delta & -\gamma_0 f(\theta \vec{\zeta} \times \vec{K}_{d\mu}) \\ -\gamma_0 f^*(\theta \vec{\zeta} \times \vec{K}_{d\mu}) & \Delta \end{pmatrix}, \quad (\text{C7})$$

where  $\Delta$  is potential difference between the two layers (layer 1 is in potential 0 and layer 2 is in potential  $\Delta$ ),  $\gamma_0$  is the next-nearest-neighbor hopping, and

$$f(\theta \vec{\zeta} \times \vec{K}_{d\mu}) = 2 \sin \frac{\pi\theta}{\sqrt{3}} \exp i \left( \theta_\mu + \frac{\pi}{2} \varepsilon_\theta + \alpha_-(\theta) \right), \quad (\text{C8})$$

with  $\varepsilon_\theta = \text{sgn}(\theta)$  and  $\alpha_-(\theta) = 2\pi\theta/\sqrt{3}$ . Note that this matrix is evaluated at  $\theta \vec{\zeta} \times \vec{K}_{d\mu}$ . Indeed, for  $\vec{k}$  sufficiently close to Dirac point  $\vec{k}$ , because  $\hbar v(\|\vec{k} - \vec{K}_d\|) \ll \gamma_0 |f(\theta \vec{\zeta} \times \vec{K}_{d\mu})|$ , we can neglect the dependence on  $\vec{k}$  in  $H_2$ ,  $\mathcal{G}_2$  and  $\tilde{\Sigma}_2(z)$ . This corresponds to the general conditions of validity of the present perturbation theory (see above the introduction to Appendix C).

So now, after some calculations, we get for the self-energy

$$\tilde{\Sigma}_0(z) = \sigma(z) \mathbf{I}, \quad (\text{C9})$$

with

$$\sigma(z) \simeq \frac{\theta_0^2}{\theta^2} \left[ \Delta - z \right], \quad (\text{C10})$$

where we have introduced  $\theta_0$ :

$$\theta_0 = \frac{3}{\sqrt{2}\pi} \frac{t}{\gamma_0}. \quad (\text{C11})$$

Using the values of  $t \simeq t_1 \simeq 0.12$  eV (Appendix B 1) and  $\gamma_0 \simeq 2.7$  eV, one finds that the value of the angle  $\theta_0$  is  $\theta_0 \simeq 1.7^\circ$ .

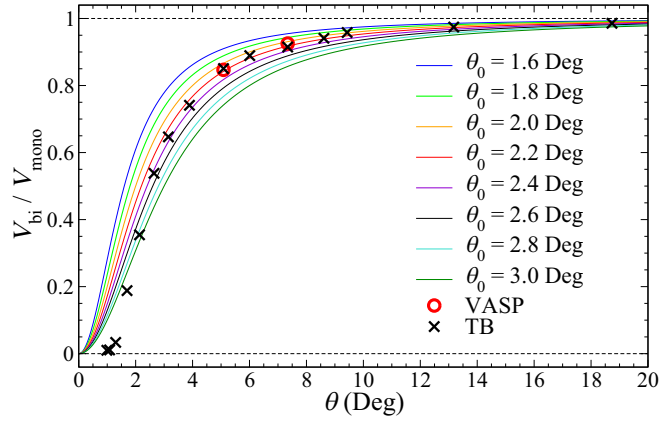


FIG. 11. Velocity ratio  $v_r/v = V_{bi}/V_{mono}$  for commensurate  $(n, m)$  bilayer cell versus rotation angle  $\theta$ , computed from Eq. (C11) with various  $\theta_0$  values. Circle, DFT calculation using VASP code; cross, TB calculations, from Ref. [3].

### 3. Velocity renormalization

The eigenvalues are the poles of the Green's function. Therefore, the energy  $E(\vec{k})$  is given by

$$E - \sigma(E) = \pm \hbar v |\delta \vec{k}|. \quad (C12)$$

For  $|\vec{k}| = 0$ , we have solution  $E = E_0$  such that

$$E_0 - \sigma(E_0) = 0. \quad (C13)$$

For small  $\vec{k}$ , we can write  $E(\vec{k}) = E_0 + \delta E(\vec{k})$ . Eventually, we have a nice formula:

$$\delta E = \frac{\pm \hbar v |\delta \vec{k}|}{1 - \sigma'(E_0)}. \quad (C14)$$

Finally, the renormalized velocity  $v_r$  is

$$\frac{v_r}{v} = \frac{1}{1 + \theta_0^2/\theta^2}. \quad (C15)$$

Therefore, using a well-established TB model, we recover velocity renormalization consistent with that of Refs. [2,15]. In addition, we find that this velocity renormalization is independent of the difference in potential of two layers. As shown in Fig. 11, a systematic study of the renormalization of the velocity close to the Dirac point is done [3], compared to its value in a monolayer graphene, for rotation angles  $\theta$  varying between  $0^\circ$  and  $60^\circ$  (Fig. 11). The renormalization of the velocity varies symmetrically around  $\theta = 30^\circ$ . Indeed, the two limit cases  $\theta = 0^\circ$  (AA stacking) and  $\theta = 60^\circ$  (AB stacking) are different, but Moiré patterns when  $\theta \rightarrow 0^\circ$  and when  $\theta \rightarrow 60^\circ$  are similar because a simple translation by a vector transforms an AA zone to an AB zone.

Focusing on angles smaller than  $30^\circ$ , three regimes can be defined [3] as a function of the rotation angle  $\theta$  (Fig. 11). For large  $\theta$  ( $20^\circ \leq \theta \leq 30^\circ$ ), the Fermi velocity is very close to that of graphene. For intermediate values of  $\theta$  ( $3^\circ \leq \theta \leq 20^\circ$ ), the velocity renormalization is predicted by Eq. (C15), as well as by the perturbative theory of Lopes dos Santos *et al.* [15] For the small rotation angles ( $\theta < 2^\circ$ ), a new regime occurs where the velocity tends to zero and perturbation theory cannot be applied.

### 4. Electron lifetime

The two layers of the tBLG can have a very different amount of disorder due to their different exposures to environment. For example, the lower layer will be in contact with a substrate and the upper layer is exposed either to vacuum or to a gas (sensor application). Therefore, it is of high interest to consider the limiting case where defects are present in one layer and absent from the other layer. In the following, we consider that defects are present only in layer 2. If the two layers were decoupled, defects in one layer would affect the electron lifetime in that layer but not in the other one. Since the layers are coupled, defects in one layer will also affect the electronic lifetime in the other layer. In this Appendix section, we discuss how such a distribution of defects impacts the electron lifetime.

If there is disorder in the lower layer (layer 2), the Bloch states of this layer will have a contribution to their self-energy which is imaginary. This can be represented in the simplest possible model by a purely imaginary part of the potential energy  $\Delta$ ,

$$\Delta = -\frac{i\hbar}{\tau_2}, \quad (C16)$$

where  $\tau_2$  is the lifetime in layer 2 due to disorder in layer 2. Using formula Eq. (C10), we see that electrons in layer 1 acquire an imaginary self-energy:

$$\Im \sigma(z) = -\frac{i\hbar}{\tau_1} = -\frac{i\hbar \theta_0^2}{\tau_2 \theta^2}. \quad (C17)$$

Therefore, the lifetimes  $\tau_1$  and  $\tau_2$  in layer 1 and layer 2 are related through

$$\frac{\tau_1}{\tau_2} = \left(\frac{\theta}{\theta_0}\right)^2, \quad (C18)$$

where  $\theta_0$  is given by Eq. (C11) and is the same quantity as in the velocity renormalization expression Eq. (C15).

### 5. Spatial variation of density of states

As explained above, the coupling between Bloch states of different wave vectors in layer 1 (due to interlayer coupling with layer 2) corresponds to the selection rule

$$\delta \vec{k}_f \simeq \delta \vec{k}_0 + \vec{G}_k, \quad (C19)$$

where  $\vec{G}_k = \theta \vec{\zeta} \times (\vec{K}_{Di} - \vec{K}_{Dj})$  is a reciprocal lattice vector of the Moiré lattice. The typical difference in energy between Bloch states of  $\delta \vec{k}_f$  and of  $\delta \vec{k}_0$  is  $\Delta E \simeq \hbar v \theta |\vec{K}_{Di}|$ . This difference is nearly independent of  $\delta \vec{k}_0$  provided that it is sufficiently close to zero. The typical coupling is  $t_{eff} \simeq t^2/(\hbar v \theta |\vec{K}_{Di}|)$ .

Then the mixing between states of wave vector close to  $(\vec{K}_{Di})$  and wave vector close to  $\vec{K}_{Di} + \vec{G}_k$  will be of order  $t_{eff}/\Delta E$ , i.e., of order  $(\theta_1/\theta)^2$ . Therefore, the relative variation of the DOS of a state is independent of the energy, for states sufficiently close to the Dirac point, and it depends only on the position in the Moiré pattern. A precise calculation [74]

provides the expression given in the main text [Eq. (2)],

$$\frac{\Delta\rho(E, \vec{r})}{\rho_m(E)} \simeq \left(\frac{\theta_1}{\theta}\right)^2 \sum_{j=1}^6 \cos(\vec{G}_j \cdot \vec{r}), \quad (\text{C20})$$

where  $\vec{G}_j$  are six equivalent vectors of the reciprocal space of the Moiré lattice and where the rotation angle  $\theta_1$  is given by

$$\theta_1 = \frac{\sqrt{2}t}{(\hbar v K_D)} = \frac{\theta_0}{\sqrt{3}}. \quad (\text{C21})$$

Using the interlayer coupling value  $t \simeq 0.12$  eV (Appendix B 1) one finds that  $\theta_1$  is close to one degree.

We emphasize that the present theory is perturbative in the coupling  $t$ . This perturbation theory is valid for sufficiently large values of  $\theta$  as explained in the introduction of Appendix C. The other assumption is to neglect Fourier components of the interlayer Hamiltonian that couple a Bloch state to other states having wave vectors away from the Dirac cones. This approximation can lead to the underestimation of modulations of the DOS at high spatial frequencies with respect to the Moiré period. This could explain why the DOS modulation (TB calculations) on sublattices A and B can differ by about  $\pm 15\%$  as compared to averaged DOS, whereas the present perturbative theory does not predict this difference. Note that the average DOS of two neighboring A and B atoms is well reproduced by the analytical model.

- 
- [1] A. K. Geim and I. V. Grigorieva, Van der Waals heterostructures, *Nature* **499**, 419 (2013).
- [2] J. M. B. Lopes dos Santos, N. M. R. Peres, and A. H. Castro Neto, Graphene Bilayer with a Twist: Electronic Structure, *Phys. Rev. Lett.* **99**, 256802 (2007).
- [3] G. Trambly de Laissardière, D. Mayou, and L. Magaud, Localization of dirac electrons in rotated graphene bilayers, *Nano Lett.* **10**, 804 (2010).
- [4] E. Suárez Morell, J. D. Correa, P. Vargas, M. Pacheco, and Z. Barticevic, Flat bands in slightly twisted bilayer graphene: Tight-binding calculations, *Phys. Rev. B* **82**, 121407(R) (2010).
- [5] R. Bistritzer and A. H. MacDonald, Transport between twisted graphene layers, *Phys. Rev. B* **81**, 245412 (2010).
- [6] R. Bistritzer and A. H. MacDonald, Moiré bands in twisted double-layer graphene, *Proc. Natl. Acad. Sci.* **108**, 12233 (2011).
- [7] G. Trambly de Laissardière, D. Mayou, and L. Magaud, Numerical studies of confined states in rotated bilayers of graphene, *Phys. Rev. B* **86**, 125413 (2012).
- [8] G. Li, A. Luican, J. M. B. Lopes dos Santos, A. H. Castro Neto, A. Reina, J. Kong, and E. Y. Andrei, Observation of Van Hove singularities in twisted graphene layers, *Nat. Phys.* **6**, 109 (2009).
- [9] A. Luican, G. Li, A. Reina, J. Kong, R. R. Nair, K. S. Novoselov, A. K. Geim, and E. Y. Andrei, Single-Layer Behavior and Its Breakdown in Twisted Graphene Layers, *Phys. Rev. Lett.* **106**, 126802 (2011).
- [10] I. Brihuega, P. Mallet, H. González-Herrero, G. Trambly de Laissardière, M. M. Ugeda, L. Magaud, J. M. Gómez-Rodríguez, F. Ynduráin, and J.-Y. Veuillen, Unraveling the Intrinsic and Robust Nature of Van Hove Singularities in Twisted Bilayer Graphene by Scanning Tunneling Microscopy and Theoretical Analysis, *Phys. Rev. Lett.* **109**, 196802 (2012).
- [11] L. Huder, A. Artaud, T. Le Quang, G. T. de Laissardière, A. G. M. Jansen, G. Lapertot, C. Chapelier, and V. T. Renard, Electronic Spectrum of Twisted Graphene Layers Under Heterostrain, *Phys. Rev. Lett.* **120**, 156405 (2018).
- [12] Y. Cao, V. Fatemi, A. Demir, S. Fang, S. L. Tomarken, J. Y. Luo, J. D. Sanchez-Yamagishi, K. Watanabe, T. Taniguchi, E. Kaxiras, R. C. Ashoori, and P. Jarillo-Herrero, Correlated insulator behavior at half-filling in magic-angle graphene superlattices, *Nature* **556**, 80 (2018).
- [13] Y. Cao, V. Fatemi, S. Fang, K. Watanabe, T. Taniguchi, E. Kaxiras, and P. Jarillo-Herrero, Unconventional superconductivity in magic-angle graphene superlattices, *Nature* **556**, 43 (2018).
- [14] S. Latil, V. Meunier, and L. Henrard, Massless fermions in multilayer graphitic systems with misoriented layers: *Ab initio* calculations and experimental fingerprints, *Phys. Rev. B* **76**, 201402(R) (2007).
- [15] J. M. B. Lopes dos Santos, N. M. R. Peres, and A. H. Castro Neto, Continuum model of the twisted graphene bilayer, *Phys. Rev. B* **86**, 155449 (2012).
- [16] G. Trambly de Laissardière, O. F. Namarvar, D. Mayou, and L. Magaud, Electronic properties of asymmetrically doped twisted graphene bilayers, *Phys. Rev. B* **93**, 235135 (2016).
- [17] T. Chari, R. Ribeiro-Palau, C. R. Dean, and K. Shepard, Resistivity of rotated graphite-graphene contacts, *Nano Lett.* **16**, 4477 (2016).
- [18] H. A. Le and V. N. Do, Electronic structure and optical properties of twisted bilayer graphene calculated via time evolution of states in real space, *Phys. Rev. B* **97**, 125136 (2018).
- [19] T.-F. Chung, Y. Xu, and Y. P. Chen, Transport measurements in twisted bilayer graphene: Electron-phonon coupling and Landau level crossing, *Phys. Rev. B* **98**, 035425 (2018).
- [20] X. Wu, Y. Chuang, A. Contino, B. Sorée, S. Brems, Z. Tokei, M. Heyns, C. Huyghebaert, and I. Asselberghs, Boosting carrier mobility of synthetic few layer graphene on SiO<sub>2</sub> by interlayer rotation and decoupling, *Adv. Mater. Interfaces* **5**, 1800454 (2018).
- [21] R. Ribeiro-Palau, C. Zhang, K. Watanabe, T. Taniguchi, J. Hone, and C. R. Dean, Twistable electronics with dynamically rotatable heterostructures, *Science* **361**, 690 (2018).
- [22] M. Anđelković, L. Covaci, and F. M. Peeters, DC conductivity of twisted bilayer graphene: Angle-dependent transport properties and effects of disorder, *Phys. Rev. Mater.* **2**, 034004 (2018).
- [23] J. W. Jeon, H. Kim, H. Kim, S. Choi, and B. H. Kim, Experimental evidence for interlayer decoupling distance of twisted bilayer graphene, *AIP Adv.* **8**, 075228 (2018).
- [24] P. Rickhaus, J. Wallbank, S. Slizovskiy, R. Pisoni, H. Overweg, Y. Lee, M. Eich, M.-H. Liu, K. Watanabe, T. Taniguchi, T. Ihn, and K. Ensslin, Transport through a network of topological channels in twisted bilayer graphene, *Nano Lett.* **18**, 6725 (2018).

- [25] V. N. Do, H. A. Le, and D. Bercioux, Time-evolution patterns of electrons in twisted bilayer graphene, *Phys. Rev. B* **99**, 165127 (2019).
- [26] G. Sharma, I. Yudhistira, N. Chakraborty, D. Y. H. Ho, M. S. Fuhrer, G. Vignale, and S. Adam, Carrier transport theory for twisted bilayer graphene in the metallic regime, [arXiv:2003.00018](https://arxiv.org/abs/2003.00018).
- [27] F. Hidalgo, A. Rubio-Ponce, and C. Noguez, Tuning adsorption of methylamine and methanethiol on twisted-bilayer graphene, *J. Phys. Chem. C* **123**, 15273 (2019).
- [28] J. Katoch, T. Zhu, D. Kochan, S. Singh, J. Fabian, and R. K. Kawakami, Transport Spectroscopy of Sublattice-Resolved Resonant Scattering in Hydrogen-Doped Bilayer Graphene, *Phys. Rev. Lett.* **121**, 136801 (2018).
- [29] A. K. M. Pinto, N. F. Frazão, D. L. Azevedo, and F. Moraes, Evidence for flat zero-energy bands in bilayer graphene with a periodic defect lattice, *Physica E: Low-dimensional Systems and Nanostructures* **119**, 113987 (2020).
- [30] T. Ohta, A. Bostwick, T. Seyller, K. Horn, and E. Rotenberg, Controlling the electronic structure of bilayer graphene, *Science* **313**, 951 (2006), <http://science.sciencemag.org/content/313/5789/951.full.pdf>.
- [31] C. Coletti, C. Riedl, D. S. Lee, B. Krauss, L. Patthey, K. von Klitzing, J. H. Smet, and U. Starke, Charge neutrality and band-gap tuning of epitaxial graphene on sic by molecular doping, *Phys. Rev. B* **81**, 235401 (2010).
- [32] I. Brihuega, P. Mallet, C. Bena, S. Bose, C. Michaelis, L. Vitali, F. Varchon, L. Magaud, K. Kern, and J. Y. Veuillen, Quasiparticle Chirality in Epitaxial Graphene Probed at the Nanometer Scale, *Phys. Rev. Lett.* **101**, 206802 (2008).
- [33] J. Hass, R. Feng, T. Li, X. Li, Z. Zong, W. A. de Heer, P. N. First, E. H. Conrad, C. A. Jeffrey, and C. Berger, Highly ordered graphene for two dimensional electronics, *Appl. Phys. Lett.* **89**, 143106 (2006).
- [34] J. Hass, W. A. de Heer, and E. H. Conrad, The growth and morphology of epitaxial multilayer graphene, *J. Phys.: Condens. Matter* **20**, 323202 (2008).
- [35] K. V. Emtsev, F. Speck, Th. Seyller, L. Ley, and J. D. Riley, Interaction, growth, and ordering of epitaxial graphene on sic0001 surfaces: A comparative photoelectron spectroscopy study, *Phys. Rev. B* **77**, 155303 (2008).
- [36] J. Hass, F. Varchon, J. E. Millán-Otoya, M. Sprinkle, N. Sharma, W. A. de Heer, C. Berger, P. N. First, L. Magaud, and E. H. Conrad, Why Multilayer Graphene on *4h*-SiC(000 $\bar{1}$ ) Behaves Like a Single Sheet of Graphene, *Phys. Rev. Lett.* **100**, 125504 (2008).
- [37] M. Sprinkle, D. Siegel, Y. Hu, J. Hicks, A. Tejada, A. Taleb-Ibrahimi, P. Le Fèvre, F. Bertran, S. Vizzini, H. Enriquez, S. Chiang, P. Soukiassian, C. Berger, W. A. de Heer, A. Lanzara, and E. H. Conrad, First Direct Observation of a Nearly Ideal Graphene Band Structure, *Phys. Rev. Lett.* **103**, 226803 (2009).
- [38] J. Hicks, M. Sprinkle, K. Shepperd, F. Wang, A. Tejada, A. Taleb-Ibrahimi, F. Bertran, P. Le Fèvre, W. A. de Heer, C. Berger, and E. H. Conrad, Symmetry breaking in commensurate graphene rotational stacking: Comparison of theory and experiment, *Phys. Rev. B* **83**, 205403 (2011).
- [39] S. Latil and L. Henrard, Charge Carriers in Few-Layer Graphene Films, *Phys. Rev. Lett.* **97**, 036803 (2006).
- [40] F. Varchon, P. Mallet, J.-Y. Veuillen, and L. Magaud, Ripples in epitaxial graphene on the si-terminated SiC(0001) surface, *Phys. Rev. B* **77**, 235412 (2008).
- [41] F. Zhang, B. Sahu, H. Min, and A. H. MacDonald, Band structure of ABC-stacked graphene trilayers, *Phys. Rev. B* **82**, 035409 (2010).
- [42] E. McCann and M. Koshino, The electronic properties of bilayer graphene, *Rep. Prog. Phys.* **76**, 056503 (2013).
- [43] A. V. Rozhkov, A. O. Sboychakov, A. L. Rakhmanov, and F. Nori, Electronic properties of graphene-based bilayer systems, *Phys. Rep.* **648**, 1 (2016).
- [44] D. L. Miller, K. D. Kubista, G. M. Rutter, M. Ruan, W. A. de Heer, P. N. First, and J. A. Stroscio, Observing the quantization of zero mass carriers in graphene, *Science* **324**, 924 (2009).
- [45] C. Berger, Z. Song, X. Li, X. Wu, N. Brown, C. Naud, D. Mayou, T. Li, J. Hass, A. N. Marchenkov, E. H. Conrad, P. N. First, and W. A. de Heer, Electronic confinement and coherence in patterned epitaxial graphene, *Science* **312**, 1191 (2006).
- [46] M. L. Sadowski, G. Martinez, M. Potemski, C. Berger, and W. A. de Heer, Landau Level Spectroscopy of Ultrathin Graphite Layers, *Phys. Rev. Lett.* **97**, 266405 (2006).
- [47] T. Ohta, J. T. Robinson, P. J. Feibelman, A. Bostwick, E. Rotenberg, and T. E. Beechem, Evidence for Interlayer Coupling and Moiré Periodic Potentials in Twisted Bilayer Graphene, *Phys. Rev. Lett.* **109**, 186807 (2012).
- [48] V. Cherkaz, G. Trambly de Laissardière, P. Mallet, and J.-Y. Veuillen, Van Hove singularities in doped twisted graphene bilayers studied by scanning tunneling spectroscopy, *Phys. Rev. B* **91**, 155428 (2015).
- [49] P. Lazar, F. Karlický, P. Jurečka, M. Kocman, E. Otyepková, K. Šafářová, and M. Otyepka, Adsorption of small organic molecules on graphene, *J. Am. Chem. Soc.* **135**, 6372 (2013).
- [50] I. Brihuega and F. Yndurain, Selective hydrogen adsorption in graphene rotated bilayers, *J. Phys. Chem. B* **122**, 595 (2018).
- [51] A. H. Castro Neto, F. Guinea, N. M. R. Peres, K. S. Novoselov, and A. K. Geim, The electronic properties of graphene, *Rev. Mod. Phys.* **81**, 109 (2009).
- [52] G. Trambly de Laissardière and D. Mayou, Conductivity of Graphene with Resonant and Nonresonant Adsorbates, *Phys. Rev. Lett.* **111**, 146601 (2013).
- [53] A. Missaoui, J. J. Khabthani, N.-E. Jaidane, D. Mayou, and G. Trambly de Laissardière, Numerical analysis of electronic conductivity in graphene with resonant adsorbates: comparison of monolayer and Bernal bilayer, *Eur. Phys. J. B* **90**, 75 (2017).
- [54] R. R. Nair, M. Sepioni, I.-L. Tsai, O. Lehtinen, J. Keinonen, A. V. Krasheninnikov, T. Thomson, A. K. Geim, and I. V. Grigorieva, Spin-half paramagnetism in graphene induced by point defects, *Nat. Phys.* **8**, 199 (2012).
- [55] W. L. Scopel, W. S. Paz, and J. C. C. Freitas, Interaction between single vacancies in graphene sheet: An ab initio calculation, *Solid State Commun.* **240**, 5 (2016).
- [56] D. Tománek, S. G. Louie, H. J. Mamin, D. W. Abraham, R. E. Thomson, E. Ganz, and J. Clarke, Theory and observation of highly asymmetric atomic structure in scanning-tunneling-microscopy images of graphite, *Phys. Rev. B* **35**, 7790(R) (1987).
- [57] V. M. Pereira, F. Guinea, J. M. B. Lopes dos Santos, N. M. R. Peres, and A. H. Castro Neto, Disorder Induced Localized States in Graphene, *Phys. Rev. Lett.* **96**, 036801 (2006).

- [58] V. M. Pereira, J. M. B. Lopes dos Santos, and A. H. Castro Neto, Modeling disorder in graphene, *Phys. Rev. B* **77**, 115109 (2008).
- [59] T. O. Wehling, S. Yuan, A. I. Lichtenstein, A. K. Geim, and M. I. Katsnelson, Resonant Scattering by Realistic Impurities in Graphene, *Phys. Rev. Lett.* **105**, 056802 (2010).
- [60] G. Trambly de Laissardière and D. Mayou, Conductivity of graphene with resonant adsorbates: Beyond the nearest neighbor hopping model, *Adv. Nat. Sci.: Nanosci. Nanotechnol.* **5**, 015007 (2014).
- [61] Z. Fan, A. Uppstu, and A. Harju, Anderson localization in two-dimensional graphene with short-range disorder: One-parameter scaling and finite-size effects, *Phys. Rev. B* **89**, 245422 (2014).
- [62] A. Missaoui, J. J. Khabthani, N.-E. Jaidane, D. Mayou, and G. T. de Laissardière, Mobility gap and quantum transport in a functionalized graphene bilayer, *J. Phys.: Condens. Matter* **30**, 195701 (2018).
- [63] D. Mayou, Calculation of the conductivity in the short-mean-free-path regime, *Europhys. Lett.* **6**, 549 (1988).
- [64] D. Mayou and S. N. Khanna, A real-space approach to electronic transport, *J. Phys. I (France)* **5**, 1199 (1995).
- [65] S. Roche and D. Mayou, Conductivity of Quasiperiodic Systems: A Numerical Study, *Phys. Rev. Lett.* **79**, 2518 (1997).
- [66] S. Roche and D. Mayou, Formalism for the computation of the RKKY interaction in aperiodic systems, *Phys. Rev. B* **60**, 322 (1999).
- [67] F. Triozon, J. Vidal, R. Mosseri, and D. Mayou, Quantum dynamics in two- and three-dimensional quasiperiodic tilings, *Phys. Rev. B* **65**, 220202(R) (2002).
- [68] P. A. Lee and T. V. Ramakrishnan, Disordered electronic systems, *Rev. Mod. Phys.* **57**, 287 (1985).
- [69] G. Trambly de Laissardière and D. Mayou, Electronic transport in graphene: Quantum effects and role of local defects, *Mod. Phys. Lett. B* **25**, 1019 (2011).
- [70] S. Shallcross, S. Sharma, and O. A. Pankratov, Quantum Interference at the Twist Boundary in Graphene, *Phys. Rev. Lett.* **101**, 056803 (2008).
- [71] E. J. Mele, Commensuration and interlayer coherence in twisted bilayer graphene, *Phys. Rev. B* **81**, 161405(R) (2010).
- [72] A. O. Sboychakov, A. L. Rakhmanov, A. V. Rozhkov, and F. Nori, Electronic spectrum of twisted bilayer graphene, *Phys. Rev. B* **92**, 075402 (2015).
- [73] A. V. Rozhkov, A. O. Sboychakov, A. L. Rakhmanov, and F. Nori, Single-electron gap in the spectrum of twisted bilayer graphene, *Phys. Rev. B* **95**, 045119 (2017).
- [74] O. F. Namarvar, Electronic structure and quantum transport in graphene nanostructures, Ph.D. thesis, Université de Grenoble, France, 2012.